PHYSICAL REVIEW B **80**, 045410 (2009)

Character of electronic states in graphene antidot lattices: Flat bands and spatial localization

Mihajlo Vanević,[1] Vladimir M. Stojanović,[2,3] and Markus Kindermann[1]
[1]*School of Physics, Georgia Institute of Technology, Atlanta, Georgia 30332, USA*
[2]*Department of Physics, Carnegie Mellon University, Pittsburgh, Pennsylvania 15213, USA*
[3]*Department of Physics, University of Basel, Klingelbergstrasse 82, CH-4056 Basel, Switzerland*

(Received 11 March 2009; revised manuscript received 18 June 2009; published 14 July 2009)

Graphene antidot lattices have recently been proposed as a new breed of graphene-based superlattice structures. We study electronic properties of triangular antidot lattices, with emphasis on the occurrence of dispersionless (flat) bands and the ensuing electron localization. Apart from strictly flat bands at zero energy (Fermi level), whose existence is closely related to the bipartite lattice structure, we also find quasiflat bands at low energies. We predict the real-space electron density profiles due to these localized states for a number of representative antidot lattices. We point out that the studied low-energy localized states compete with states induced by the superlattice-scale defects in this system, which have been proposed as hosts for electron-spin qubits. Furthermore, we suggest that local moments formed in these midgap zero-energy states may be at the origin of a surprising saturation of the electron dephasing length observed in recent weak localization measurements in graphene antidot lattices.

DOI: 10.1103/PhysRevB.80.045410 PACS number(s): 73.23.−b, 73.63.−b, 73.21.Cd

I. INTRODUCTION

Investigations of the electronic properties of graphene constitute a relatively new and thriving subarea of condensed-matter research.[1] After the first successful fabrication of graphene monolayers[2]—by means of a mechanical exfoliation of graphite—this two-dimensional semimetallic material has ignited tremendous experimental[3–5] and theoretical[6–15] interests. From a fundamental standpoint, one of the main incentives for studying graphene stems from emergent analogies between the low-energy physics of the material and relativistic quantum mechanics.[16–18] Graphene is just as interesting from a practical point of view: owing to its exceptional properties—the extremely high mobility, chemical inertness, atomic thickness, and easy control of charge carriers by applied gate voltages—it holds a great promise for a carbon-based "post-silicon" microelectronics.[19–22]

Aside from simple graphene monolayers, patterning of monolayer films by nanolithography methods[23]—allowing feature sizes as small as tens of nanometers—has led to the demonstration of nanostructures such as Hall bars,[24–26] quantum dots,[27] nanoribbons,[28–30] and Aharonov-Bohm interferometers.[31] Another family of graphene-based structures has recently been proposed—triangular superlattices of holes (antidots) cut in a graphene sheet, known as antidot lattices.[32,33] Unlike pristine graphene which is semimetallic, graphene antidot lattices are semiconducting, with a direct band gap that depends on the antidot size. Square antidot lattices have been studied experimentally quite recently, corroborating the existence of a transport gap.[34,35] In addition, the weak localization correction to the conductance and a surprising saturation of the electron dephasing length at the superlattice scale have been observed in these experiments.

In a recent work,[32] antidot lattices have been proposed as a platform for quantum computation, with defects in this system envisioned as hosts for electron-spin qubits. While the proposal of Ref. 32 focuses on localized states due to defects on the *superlattice scale* (such as missing antidots), their counterparts on the *lattice scale* (such as vacancies or adatoms), essentially unavoidable along the antidot edges of experimental samples, are known to give rise to midgap (bound) states as well.[36,37] One may thus expect that the two types of defects compete. In addition, midgap states caused by lattice-scale defects might provide a plausible explanation of the maximal dephasing length observed in the experiment of Ref. 35: for sufficiently large charging energies, such midgap states can host local (spin) moments at the antidot edges that are known to be a very effective source of electron dephasing.[38] This motivates us to systematically study midgap states in graphene antidot lattices, with a focus on their spatial profile and the corresponding dispersionless (flat) bands.

On bipartite lattices (such as graphene) which have an excess of atoms on one of the two sublattices, zero-energy states are expected on very general grounds.[39,40] As a consequence, midgap states may exist even in perfectly symmetric and periodic antidot lattices. This was put forward by Shima and Aoki[41] in a general symmetry-based classification of superhoneycomb systems (i.e., triangular superlattices based on an underlying honeycomb lattice). Generically, however, midgap states will be introduced by irregularities in the shape of the antidot lattice on the atomic scale, which are unavoidable in present-day experiments. We analyze the resulting band structure and the spatial profile of the corresponding wave functions for a number of representative antidot lattices. Furthermore, we determine low-energy tunneling-current distributions that can be compared with scanning tunneling microscopy (STM) measurements. Our estimates for the charging energies of the predicted zero-energy states indeed suggest that for typical experimental parameters such states can form local moments and thus provide strong dephasing upon electron scattering from the antidot edges.

The remainder of the paper is organized as follows. In Sec. II, we first briefly introduce the graphene superlattices of interest, accompanied by the notation and conventions to

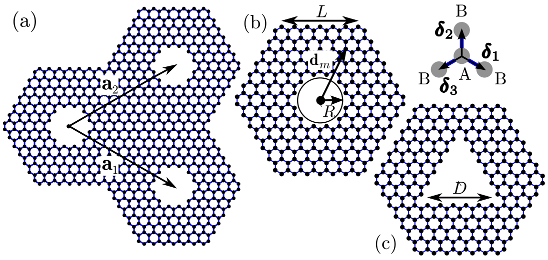

FIG. 1. (Color online) Graphene antidot lattice: (a) Lattice structure described by the basis vectors $\mathbf{a}_1$ and $\mathbf{a}_2$, with magnitude $|\mathbf{a}_1| = |\mathbf{a}_2| = La\sqrt{3}$; (b) hexagonal unit cell with a circular antidot; and (c) hexagonal unit cell with a triangular antidot. Vectors $\boldsymbol{\delta}_1, \boldsymbol{\delta}_2, \boldsymbol{\delta}_3$ specify positions of the nearest neighbors of a carbon atom on sublattice A.

be used throughout (Sec. II A), and then lay out the framework for calculating their band structure (Sec. II B) and the tunneling-current distribution (Sec. II C). The obtained results are presented and discussed in view of the generic properties of the superhoneycomb and bipartite systems in Sec. III. Finally, we summarize our findings and conclude in Sec. IV.

II. DESCRIPTION OF ANTIDOT LATTICES

A. Structure and nomenclature

To set the stage, in this section we introduce graphene antidot lattices. A segment of a typical antidot lattice with a circular perforation is depicted in Fig. 1(a), with lattice-basis vectors denoted by $\mathbf{a}_1$ and $\mathbf{a}_2$. Its unit cell is a hexagon with an antidot in the center [Fig. 1(b)]. We characterize the structure by the dimensionless side length of the hexagonal unit cell (L) and the radius of the antidot (R), both expressed in units of the graphene lattice constant $a = 2.46$ Å. (Note that while L is an integer, R can also take noninteger values; $a = a_{\rm cc}\sqrt{3}$, where $a_{\rm cc} = 1.42$ Å is the distance between nearest-neighbor carbon atoms.) Therefore, we use the notation $\{L,R\}$ to specify antidot lattices with circular perforations. The unit cell of an antidot lattice with a triangular perforation, which can be characterized by $\{L,D\}$ (where D is the side length of the triangle), is shown in Fig. 1(c). The number of carbon atoms (hereafter C atoms) per unit cell of an antidot lattice will henceforth be denoted by $N_{\rm C}$.

If we take a C atom on sublattice A at the origin, its nearest neighbors are determined by vectors $\boldsymbol{\delta}_1 = (\sqrt{3}/2, -1/2)a_{\rm cc}$, $\boldsymbol{\delta}_2 = (0,1)a_{\rm cc}$, and $\boldsymbol{\delta}_3 = (-\sqrt{3}/2, -1/2)a_{\rm cc}$ (see Fig. 1). Alternatively, for a C atom on sublattice B at origin, the corresponding vectors are $-\boldsymbol{\delta}_1$, $-\boldsymbol{\delta}_2$, and $-\boldsymbol{\delta}_3$.

B. Method for band-structure calculation

Given the large size of the unit cells in our superlattice—that in the cases of practical interest, with antidot diameter larger than about 10 nm, have numbers of C atoms in excess of several thousands—a band-structure calculation using the standard *ab initio* methods based on the density functional theory (DFT) is not feasible. We thus compute the electronic band structure of graphene antidot lattices within a π-orbital tight-binding model. This method is known to reproduce very accurately the low-energy part of the DFT band structure of pristine graphene.[42]

The tight-binding Hamiltonian of an antidot lattice reads

$$\hat{H}_{\rm e} = -\frac{t}{2}\sum_{\mathbf{R},m,\boldsymbol{\delta}} (\hat{a}^{\dagger}_{\mathbf{R}+\mathbf{d}_m+\boldsymbol{\delta}}\hat{a}_{\mathbf{R}+\mathbf{d}_m} + \text{H.c.}), \qquad (1)$$

where vectors $\mathbf{R}$ designate unit cells (in total N of them), $\mathbf{d}_m (m = 1, \ldots, N_{\rm C})$ specify positions of C atoms within a unit cell, $\boldsymbol{\delta}$ stands for nearest neighbors of a C atom at position $\mathbf{R}+\mathbf{d}_m$, and $t \approx 2.8$ eV is the nearest-neighbor hopping matrix element, while the factor 1/2 is needed to correct for double counting. After Fourier transformation to momentum space, the band-structure calculation amounts to a sparse-matrix diagonalization problem of dimension $N_{\rm C}$.

The Bloch wave functions corresponding to the energy eigenvalues $\mathcal{E}_{n\alpha}(\mathbf{k})$ are given by $\psi_{n\mathbf{k}\alpha}(\mathbf{r}) = \Sigma_m C_m^{(n\mathbf{k}\alpha)}\phi_{m\mathbf{k}}(\mathbf{r})$, where $\phi_{m\mathbf{k}}(\mathbf{r}) = N^{-1/2}\Sigma_{\mathbf{R}} e^{i\mathbf{k}\cdot\mathbf{R}}\varphi(\mathbf{r}-\mathbf{R}-\mathbf{d}_m)$. Here n enumerates energy bands (with possible additional degeneracy labeled by α) and $\varphi(\mathbf{r})$ denotes the $2p_z$ orbital of a C atom. The energy-eigenvalue problem $\hat{H}|\psi_{\mathbf{k}}\rangle = \mathcal{E}|\psi_{\mathbf{k}}\rangle$ reduces to $\det[\mathbf{H}(\mathbf{k}) - \mathcal{E}\mathbf{S}(\mathbf{k})] = 0$, with matrices $\mathbf{H}$ and $\mathbf{S}$ given by $H_{mm'}(\mathbf{k}) = \langle \phi_{m\mathbf{k}}|\hat{H}|\phi_{m'\mathbf{k}}\rangle$ and $S_{mm'}(\mathbf{k}) = \langle \phi_{m\mathbf{k}}|\phi_{m'\mathbf{k}}\rangle$, respectively. In the nearest-neighbor approximation,

$$H_{mm'}(\mathbf{k}) = -t\left(\delta_{\langle \mathbf{d}_m,\mathbf{d}_{m'}\rangle} + \sum_{\mathbf{R}} e^{i\mathbf{k}\cdot\mathbf{R}}\delta_{\langle \mathbf{d}_m,\mathbf{d}_{m'}+\mathbf{R}\rangle}\right), \qquad (2)$$

where the summation runs over superlattice vectors $\mathbf{R} = \pm\mathbf{a}_1, \pm\mathbf{a}_2, \pm(\mathbf{a}_1-\mathbf{a}_2)$ (only neighboring unit cells contribute) and $\delta_{\langle \mathbf{r},\mathbf{r}'\rangle} = 1$ if C atoms at positions $\mathbf{r}$ and $\mathbf{r}'$ are nearest neighbors, while $\delta_{\langle \mathbf{r},\mathbf{r}'\rangle} = 0$ otherwise. To a good approximation, the overlap of $2p_z$ orbitals on different C atoms can be neglected, so that $S_{mm'}(\mathbf{k}) = \delta_{mm'}$. This is a standard practice in the analyses of π-electron systems.[43]

For later reference, we describe a construction of an orthonormal eigenbasis $\{\psi_{n\mathbf{k}\alpha}\}$ of $\hat{H}$. To that end, we first note that $\phi_{m\mathbf{k}}$ form an orthonormal set: $\langle \phi_{m\mathbf{k}}|\phi_{m'\mathbf{k}'}\rangle = \delta_{mm'}\delta_{\mathbf{k}\mathbf{k}'}$. [For $\mathbf{k} = \mathbf{k}'$, the orthogonality follows from $S_{mm'}(\mathbf{k}) = \delta_{mm'}$, while for $\mathbf{k} \neq \mathbf{k}'$, it holds because $\phi_{m\mathbf{k}}$ and $\phi_{m'\mathbf{k}'}$ belong to different eigensubspaces of the lattice-translation operator.] This implies that $\langle \psi_{n\mathbf{k}\alpha}|\psi_{n'\mathbf{k}'\alpha'}\rangle = 0$ for $\mathbf{k} \neq \mathbf{k}'$. Therefore, to construct an orthonormal set, we find an orthonormal basis in the degenerate eigensubspaces of $\mathbf{H}(\mathbf{k})$. The orthogonality of the latter basis $\Sigma_m (C_m^{(n\mathbf{k}\alpha)})^* C_m^{(n\mathbf{k}\alpha')} = \delta_{\alpha\alpha'}$ implies that $\langle \psi_{n\mathbf{k}\alpha}|\psi_{n\mathbf{k}'\alpha'}\rangle = \delta_{\mathbf{k}\mathbf{k}'}\delta_{\alpha\alpha'}$.

C. Tunneling-current distribution

STM and related techniques are known as powerful tools for mapping out the spatial form of surface electron states.[44] In order to visualize the spatial structure of the studied low-energy states and provide the means of comparing our results to STM measurements, we predict the tunneling-current distribution.

The tunneling current

$$\mathcal{I}(\mathbf{r}) \propto \int_{\mathcal{E}_F}^{\mathcal{E}_F+eV} d\mathcal{E}\rho(\mathbf{r};\mathcal{E}), \tag{3}$$

with $\mathcal{E}_F$ being the Fermi energy and V the STM-tip bias voltage, can be used to probe the spatial dependence of the local density of states[45]

$$\rho(\mathbf{r};\mathcal{E}) = \sum_{n\mathbf{k}\alpha} |\psi_{n\mathbf{k}\alpha}(\mathbf{r})|^2 \delta[\mathcal{E}-\mathcal{E}_n(\mathbf{k})]. \tag{4}$$

This is a basis-independent quantity, expressed here in terms of an *orthonormal* eigenbasis $\{\psi_{n\mathbf{k}\alpha}\}$ of $\hat{H}$, constructed as described above. In the case that only one flat band at $\mathcal{E} = \mathcal{E}_{n_0}$ falls into the energy window in Eq. (3), we have

$$\begin{aligned}\mathcal{I}(\mathbf{r}) &\propto \sum_{\mathbf{k}\alpha} |\psi_{n_0\mathbf{k}\alpha}(\mathbf{r})|^2 \\ &= \sum_{\mathbf{k}\alpha} \sum_{mm'} (C_m^{(n_0\mathbf{k}\alpha)})^* C_{m'}^{(n_0\mathbf{k}\alpha)} \phi_{m\mathbf{k}}^*(\mathbf{r}) \phi_{m'\mathbf{k}}(\mathbf{r}).\end{aligned} \tag{5}$$

Strictly speaking, to calculate the tunneling current we would need to use the explicit form of $2p_z$ orbitals. However, Eq. (5) simplifies if we assume that the $2p_z$ orbitals are well localized on C atoms and hence neglect the overlap of the neighboring orbitals. After coarse graining $I(\mathbf{r}) = (1/\Delta V)\int_{\Delta V \ni \mathbf{r}} d^3\mathbf{r}'\mathcal{I}(\mathbf{r}')$ in the vicinity of a C atom positioned at $\mathbf{r}=\mathbf{R}+\mathbf{d}_m$, we obtain the sought-after tunneling-current distribution

$$I(\mathbf{r}) \propto \sum_{\mathbf{k}\alpha} |C_m^{(n_0\mathbf{k}\alpha)}|^2, \tag{6}$$

which is a lattice-periodic quantity.

III. RESULTS AND DISCUSSION

In this section, we investigate the band structure of antidot lattices, with emphasis on localized states at low energy. The spatial profile of these states is characterized by a tunneling-current distribution. We present results for both ideal lattices and lattices with defects (vacancies and/or debonded C atoms). Since we describe the system by a nearest-neighbor tight-binding model on a bipartite lattice, the resulting energy spectrum has particle-hole symmetry.[46] With this in mind, in the following we focus on the bands above or at the Fermi level ($\mathcal{E}=0$).

We start with an antidot lattice that is made up of perfect circular perforations, such as those considered in Ref. 32. The band structure of an $\{L=9, R=3\}$ antidot lattice is shown in Fig. 2. A band gap $\mathcal{E}_g$ opens at the Γ point ($\mathbf{k}=0$). For antidot lattices with a relatively small number of removed C atoms (N_{rem}) compared to the total number of atoms in the original unit cell ($N_{\text{total}}=N_{\text{rem}}+N_C$), the band gap has been predicted to scale as[32] $\mathcal{E}_g \propto \sqrt{N_{\text{rem}}}/N_{\text{total}}$. It has been demonstrated that localized states with energy inside the gap can be induced in this system by defects on the superlattice scale, e.g., missing circular antidots in the lattice.[32] Such localized states have been proposed as hosts for local spin moments that may be utilized for quantum computation. In the following, we show that these midgap states appear generically in graphene antidot lattices, even without superlattice-scale defects.

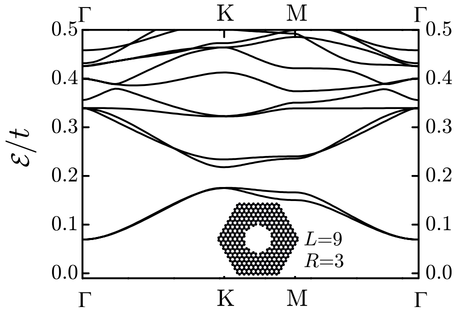

FIG. 2. (Color online) Band structure for a {9,3} antidot lattice. Only bands above the Fermi level ($\mathcal{E}=0$) are shown because of the particle-hole symmetry. Γ, K, M stand for the high-symmetry points in the Brillouin zone.

In the nearest-neighbor approximation, graphene has a bipartite lattice, that is, a lattice that can be divided into two sublattices A and B, where only sites at different sublattices are connected through nonzero hopping matrix elements. Inui *et al.*[40] showed that in such systems one has $N_A - N_B$ zero-energy states, where N_A, N_B are the total number of sites on the respective sublattices. [This result was, in fact, implicitly known even earlier: it was obtained by Lieb[39] as a prerequisite for the proof that the total spin in the exact ferromagnetic ground state of the Hubbard model on a bipartite lattice is $S=(N_A-N_B)/2$.] In a graphene superlattice with n_A and n_B sites per unit cell on A and B sublattices, respectively, these states form $n_A - n_B$ dispersionless (flat) bands at $\mathcal{E}=0$. A sublattice imbalance $n_A - n_B$ is generically introduced at the edges of graphene-based structures. Perhaps the most well-known example of the corresponding zero-energy states are the edge states in zigzag graphene ribbons that form a *partially flat* band at the Dirac point.[47,48] A pair of essentially flat (spin-polarized) bands close to the Fermi level was found also in a hydrogenated graphene ribbon, as demonstrated by *ab initio* electronic-structure calculations.[49]

In antidot lattices one expects flat bands at zero energy due to sublattice imbalances along the edges of the antidots. The sublattice imbalance can occur even for perfect regularly shaped antidots. As an example, we study antidot lattices with triangular perforations (cf. Fig. 1), which invariably have an imbalance of $n_A - n_B = D$ per antidot. Consequently, a D-fold degenerate flat band emerges at $\mathcal{E}=0$, as depicted in Fig. 3. On the other hand, it is easy to check that antidot lattices with perfect circular perforations always have $n_A = n_B$. These lattices therefore do not exhibit flat bands at $\mathcal{E}=0$ (cf. Fig. 2).

As pointed out by Inui *et al.*,[40] the single-particle states corresponding to the zero-energy flat bands are pseudospin polarized—they occupy only sites belonging to a particular sublattice. Figure 4 shows for an antidot lattice $\{L=10, D=9\}$ how this effect manifests itself in the tunneling-current distribution, which is proportional to the on-site electron density. Closer inspection reveals that the single-particle states $\psi_{\mathbf{k}}$ corresponding to the flat band at $\mathcal{E}=0$ indeed leave the B-sublattice sites unoccupied (amplitudes $C_{B_m}=0$), while the A-sublattice sites are occupied with amplitudes C_{A_m} (nor-

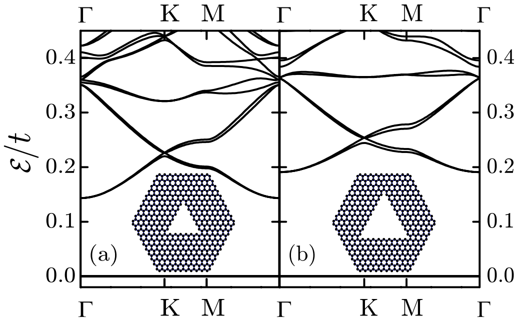

FIG. 3. (Color online) Band structure of an antidot lattice with triangular antidots. Only bands above the Fermi level ($\mathcal{E}=0$) are shown because of the particle-hole symmetry. Γ, K, M stand for the high-symmetry points in the Brillouin zone. The flat band at $\mathcal{E}=0$ is (a) sixfold degenerate ($D=6$) and (b) ninefold degenerate ($D=9$).

malized as $\Sigma_m|C_{A_m}|^2=1$), adding up to zero around each B-sublattice site [see Fig. 4(a)]. Moreover, the electronic states corresponding to the zero-energy flat bands are predominantly localized in the vicinity of the antidot edge.[50] The extent of their spatial localization is illustrated in Fig. 4(b).

It is important to emphasize that the above results are valid for an arbitrary system of bipartite structure, either of infinite or of finite size, and even in the presence of *off-diagonal* disorder and/or an external magnetic field.[40] (In the presence of a magnetic field, the hopping matrix elements become complex through the conventional Peierls substitution[51] and the particle-hole symmetry is destroyed.) Therefore, even without actual calculation, we can conclude that the discussed flat bands at $\mathcal{E}=0$ in graphene antidot lattices remain flat in a magnetic field. Analogous results for finite-size graphene antidot flakes have recently been obtained numerically.[52]

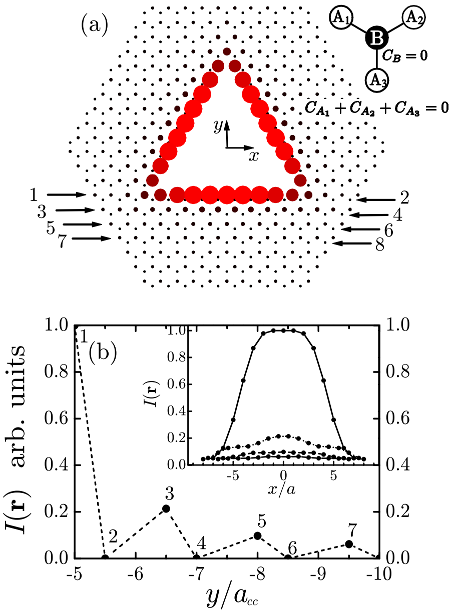

FIG. 4. (Color online) Illustration of the spatial localization of the single-particle wave function corresponding to a flat band. (a) Tunneling-current distribution $I(\mathbf{r})$, reflecting the population of only the A-sublattice sites. The sizes of the circles and the color brightness are proportional to $I(\mathbf{r})$, which is scaled to $0\leq I\leq 1$. The electron amplitudes obey the sum rule shown in the inset. (b) Tunneling-current maxima along the y direction, at positions indicated by the arrows in (a). Inset: tunneling-current distribution in the x direction.

A different perspective on the problem is furnished by a symmetry-based classification of superhoneycomb systems, as put forward by Shima and Aoki.[41] They showed that such systems can have either semiconducting (with direct band gap), semimetallic, or metallic character. This classification turns out to depend not only on the global superlattice symmetry, but also on the specific atomic configuration within the unit cell. In particular, structures with $6m$, $6m+2$, $6m+3$, and $6m+5$ (m is an integer) atoms per unit cell belong to symmetry classes designated by A_0, A_C, B_0, and B_C, respectively.[41] The respective degeneracies of the flat bands at $\mathcal{E}=0$ in these classes are $6l$, $6l\pm2$, $6l-3$, and $6l\pm1$ ($l\geq0$ is an integer). According to this classification, our antidot lattices with circular perforations belong to the A_0 type of superhoneycomb systems with $l=0$, which is consistent with the absence of flat bands at $\mathcal{E}=0$.

In realistic graphene flakes, the dangling bonds along the edges are hydrogen passivated, giving rise to an on-site potential. An on-site potential can also appear in a pure carbon system due to a weak edge magnetization induced by electron-electron interactions.[8] Since the electronic states corresponding to the zero-energy flat bands are largely localized at the antidot edges, one expects them to be strongly affected by such an edge potential. This motivates us to study the influence of an edge potential, hereafter denoted by V_e, on the zero-energy states. We assume that V_e takes nonzero values at C atoms that have only two nearest neighbors. Such a potential breaks the particle-hole symmetry of the energy spectrum by destroying the bipartite lattice structure, since it couples sites that belong to the same sublattice. However, the main effect of V_e is a lifting of the degeneracy of the zero-energy flat bands, while their dispersionless character is largely being preserved.[53] At the same time, the effect of this potential on the other bands is relatively small [cf. Figs. 5(a) and 3(b)]. This finding is indeed analogous to the behavior of flat bands in nanoribbons with hydrogenated edges, obtained using realistic first-principles DFT calculations.[49] We stress that the observed effect of the on-site potential is robust, i.e., changing the magnitude of V_e does not alter our qualitative conclusions.

In what follows we point out another generic feature of graphene antidot lattices: the occurrence of essentially flat bands at nonzero energies (even in the absence of an edge potential $V_e=0$). A characteristic example is presented in Fig. 6. While flat bands at $\mathcal{E}=0$ in bipartite lattices arise due to a global sublattice imbalance ($n_A\neq n_B$), as discussed above, we ascribe the quasiflat ones at $\mathcal{E}\neq0$ to local sublattice imbalances (while globally $n_A=n_B$). Such local imbalances can be induced even in regularly shaped antidot lattices, for instance, by debonded C atoms with a single neighbor at the edges [cf. Fig. 6(b)].

The occurrence of quasiflat bands may be understood as follows. A single debonded C atom induces a sublattice imbalance that leads to a zero-energy "defect level." One may

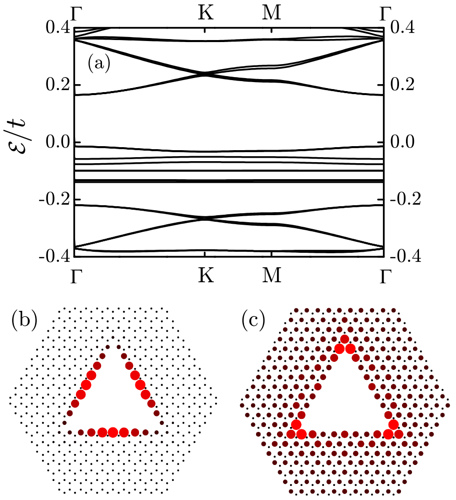

FIG. 5. (Color online) Effect of an on-site impurity potential $V_e = -0.15t$ along the antidot edges: (a) band structure and the tunneling-current distributions corresponding to (b) the lowest-lying flat band and (c) the highest flat band.

view a collection of debonded C atoms as a collection of "local sublattice imbalances" that induce one defect level each with wave functions that are localized in the vicinity of the defects. This picture is supported by the tunneling density of states shown in Fig. 6(b). Localized states induced by defects that are well separated from one another hybridize only weakly. Accordingly, these defect levels give rise to essentially dispersionless bands close to the Fermi level ($\mathcal{E} = 0$).[54] As the distance between the defects decreases, the hybridization of defect states becomes stronger and the resulting bands are shifted away from the Fermi level.

In disordered antidot lattices, debonded C atoms generically appear along the edges of irregularly shaped antidots, leading to a local sublattice imbalance. Such defects at the edge of a zigzag nanoribbon have been experimentally observed quite recently.[55] In this experiment, the multilayer graphene structures were thermally treated leading to edges that are mostly closed (i.e., folded from one layer to another). Open-edge structures with debonded C atoms are found in a local area where the folding edge is partially broken. Another source of local sublattice imbalances in disordered lattices are vacancies, for example, due to removed C atoms or C atoms that are sp^3 rehybridized as a result of hydrogen chemisorption.[56–58] In Fig. 7(a), we show that a single defect in an otherwise perfectly circular antidot lattice produces, as expected, a zero-energy band. Needless to say, in realistic disordered systems defects do not repeat with the lattice period as assumed in Fig. 7(a). Some qualitative features of realistic disordered lattices can be captured by considering a superlattice with an increased unit cell. In Fig. 7(b), we show a band structure for an antidot lattice with a unit cell containing four antidots with defects at different locations; this band structure indicates that well-separated defect states weakly hybridize, giving rise to two pairs of quasiflat bands that are symmetric with respect to the Fermi level. This suggests that for realistic disordered lattices one has a quasicontinuum of such low-energy states due to hybridization of defect states.

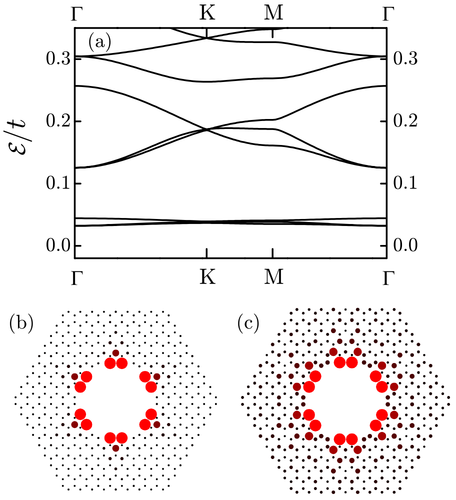

FIG. 6. (Color online) Effects of debonded C atoms in the antidot lattice {9,3.2}: (a) band structure and the tunneling-current distributions corresponding to (b) the low-lying quasiflat bands and (c) the energy bands within the range $0.125t \lesssim \mathcal{E} \lesssim 0.257t$.

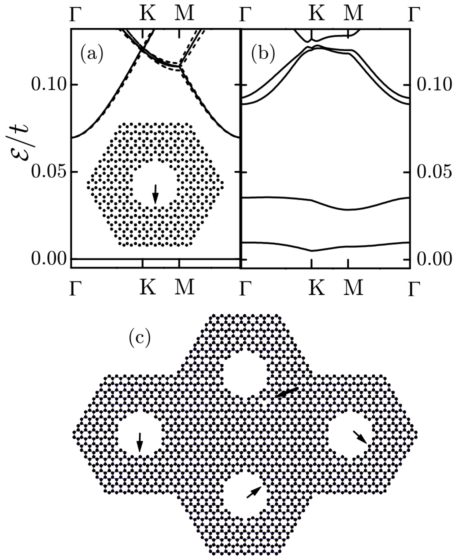

FIG. 7. (Color online) Effects of disorder in antidot lattices: (a) band structure of an antidot lattice with defects on sublattice *A* (indicated by the arrow in the inset), (b) band structure in the presence of defects on both sublattices, and (c) unit cell with arrows indicating vacancies or C adatom defects. The dashed curves in (a) represent the band structure of an ideal lattice (without disorder). Γ, *K*, *M* stand for the high-symmetry points in the Brillouin zone of the antidot lattice with the fourfold-enlarged unit cell.

We finally consider an antidot lattice with strong shape irregularities, as is likely the case in current experiments.[34,35] Although our calculation, the result of which is shown in Fig. 8, is based on periodically repeated defects, we expect that it will give reliable estimates for the localization properties of the appearing midgap states. The localization length found in this manner can be used to estimate the charging energy in the system. The obtained band structure has the expected features: the number of flat bands at $\mathcal{E} = 0$ is in agreement with general result for the bipartite systems, and

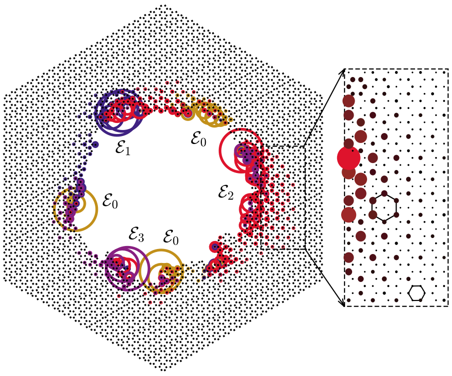

FIG. 8. (Color online) Tunneling-current distributions for a lattice with irregularly shaped antidots, shown for the four lowest electron bands: $\mathcal{E}_0=0$ (brown), $\mathcal{E}_1(\mathbf{k})$ (blue), $\mathcal{E}_2(\mathbf{k})$ (red), and $\mathcal{E}_3(\mathbf{k})$ (violet). The tunneling-current magnitudes are represented by circles of different sizes. The sublattice polarization due to edge defects, along with the accompanying charge-density reconstruction, is shown in the zoomed part of the figure.

the quasiflat bands at nonzero energies correspond to local sublattice imbalances. The electron states for both types of flat bands are localized in the vicinity of the zigzaglike segments of the antidot edges and debonded C atoms, as illustrated in Fig. 8. (In contrast to the zigzaglike segments, their armchairlike counterparts on the antidot edges do not exhibit electron localization.) Moreover, the tunneling current is maximal at the midpoints of the zigzaglike segments on the antidot edges. These features are in agreement with the existing experimental results on stepped graphite surfaces,[59] which have edges with similar irregularities.

Also depicted in Fig. 8 (see the zoomed part) is a "charge-density reconstruction" from the original graphene honeycomb lattice into a lattice with $\sqrt{3}$ times larger period, which is rotated by an angle of 30°. This is a manifestation of a Friedel-oscillation-like phenomenon, that is, a long-range electronic perturbation caused by the presence of defects. Such interference phenomena, which are essentially a consequence of the wave nature of electrons, are familiar in the context of impurities on surfaces of metals[60] and were observed on the graphite and graphene surfaces using STM.[56,61] In the case of graphene, the charge-density reconstruction results from intervalley coupling of the electronic π states. We thus conclude that there is strong intervalley scattering at the antidot edges in the lattice shown in Fig. 8. This is in agreement with the experiments of Refs. 34 and 35, where the observed weak localization (instead of weak antilocalization) is a signature of intervalley scattering at the antidot edges.

The numerically obtained localization of the induced midgap states at the antidot edges, with a localization length on the order of a few interatomic distances, suggests that the charging energies for these states can be substantial. Assuming completely random edges of length L_e, one expects $|n_A - n_B| \sim \sqrt{L_e/a}$ low-energy states per unit cell due to local sublattice imbalances (in a realistic disordered system these states will not be strictly at zero energy since the local sublattice imbalances $n_A - n_B$ in individual unit cells will partially cancel between unit cells). For the parameters in the experiment of Ref. 35, one thus expects a spacing between these localized states of about $\sqrt{L_e a} \sim 10$ nm along the edge, implying a charging energy that is substantially larger than the band gap in the system, which is roughly inversely proportional to the distance between antidots. Also, since the low-energy edge states due to local sublattice imbalances are separated by the antidot distance, one expects that their energy after hybridization is at most on the order of the band gap. Figure 7 supports this estimate. We thus conclude that the localized states observed in Fig. 8 have kinetic energies inside the band gap of the perfectly regular lattice, but charging energies that by far exceed that band gap. This suggests that local spin moments may form at the edges of disordered antidot lattices at Fermi energies where charge transport takes place. Since local magnetic moments are known to be an effective source of electron dephasing in weak localization experiments,[38] the studied midgap states offer an alternative explanation for the saturation of the electron-dephasing length at a scale corresponding to the distance between antidots reported in Ref. 35.

IV. CONCLUSIONS

In this work, we have studied the salient features of the low-energy band structure of graphene antidot lattices. Apart from strictly zero-energy (midgap) flat bands that arise from the bipartite lattice structure and a global sublattice imbalance, we have also found quasiflat bands at low, but nonzero, energies that can be ascribed to local sublattice imbalances. In addition, we have examined the influence of an edge potential on the flat bands, showing that such a potential lifts the degeneracy of these bands, without affecting significantly their dispersionless character.

We have also investigated the spatial profile of the electronic states corresponding to both classes of low-energy bands (flat and quasiflat). By analyzing the tunneling-current distributions that can be compared to STM measurements, we have demonstrated that these electronic states are generically localized at the antidot edges. The computed tunneling-current distributions also show a charge-density reconstruction from the original honeycomb lattice to a lattice with $\sqrt{3}$ times larger period and rotated through an angle of 30°. This phenomenon is indicative of intervalley scattering off irregular antidot edges, as also observed in recent experiments.[34,35]

The spatial profiles of the localized midgap states that we find allow for a rough estimate of their charging energies. That estimate suggests that such states can host local magnetic moments. We propose that such magnetic moments may be at the origin of a recently observed saturation of the dephasing length in graphene antidot lattices.[35] In addition, the investigated midgap states compete with the localized states due to superlattice-scale defects, and therefore can have significant implications for a recent proposal of spin qubits in graphene antidot lattices.[32]

ACKNOWLEDGMENTS

We acknowledge a helpful correspondence with J. Eroms and discussions with C. Flindt.

[1] For a review, see A. H. Castro Neto, F. Guinea, N. M. R. Peres, K. S. Novoselov, and A. K. Geim, Rev. Mod. Phys. **81**, 109 (2009).

[2] K. S. Novoselov, A. K. Geim, S. V. Morozov, D. Jiang, Y. Zhang, S. V. Dubonos, I. V. Grigorieva, and A. A. Firsov, Science **306**, 666 (2004).

[3] S. Y. Zhou, G. H. Gweon, A. V. Fedorov, P. N. First, W. A. de Heer, D. H. Lee, F. Guinea, A. H. Castro Neto, and A. Lanzara, Nature Mater. **6**, 770 (2007).

[4] X. Wu, X. Li, Z. Song, C. Berger, and W. A. de Heer, Phys. Rev. Lett. **98**, 136801 (2007).

[5] S. Y. Zhou, D. A. Siegel, A. V. Fedorov, F. ElGabaly, A. K. Schmid, A. H. Castro Neto, and A. Lanzara, Nature Mater. **7**, 259 (2008).

[6] J. Tworzydlo, B. Trauzettel, M. Titov, A. Rycerz, and C. W. J. Beenakker, Phys. Rev. Lett. **96**, 246802 (2006).

[7] N. M. R. Peres, A. H. Castro Neto, and F. Guinea, Phys. Rev. B **73**, 195411 (2006).

[8] Y. W. Son, M. L. Cohen, and S. G. Louie, Phys. Rev. Lett. **97**, 216803 (2006); M. Wimmer, I. Adagideli, S. Berber, D. Tománek, and K. Richter, *ibid.* **100**, 177207 (2008).

[9] V. V. Cheianov and V. I. Fal'ko, Phys. Rev. B **74**, 041403(R) (2006).

[10] M. I. Katsnelson, K. S. Novoselov, and A. K. Geim, Nat. Phys. **2**, 620 (2006).

[11] E. H. Hwang, S. Adam, and S. Das Sarma, Phys. Rev. Lett. **98**, 186806 (2007); E. H. Hwang and S. Das Sarma, Phys. Rev. B **75**, 205418 (2007).

[12] B. Trauzettel, D. V. Bulaev, D. Loss, and G. Burkard, Nat. Phys. **3**, 192 (2007).

[13] J. Milton Pereira, P. Vasilopoulos, and F. M. Peeters, Nano Lett. **7**, 946 (2007).

[14] P. Recher, B. Trauzettel, A. Rycerz, Y. M. Blanter, C. W. J. Beenakker, and A. F. Morpurgo, Phys. Rev. B **76**, 235404 (2007).

[15] T. Stauber, N. M. R. Peres, and A. H. Castro Neto, Phys. Rev. B **78**, 085418 (2008).

[16] G. W. Semenoff, Phys. Rev. Lett. **53**, 2449 (1984); D. P. DiVincenzo and E. J. Mele, Phys. Rev. B **29**, 1685 (1984).

[17] C. W. J. Beenakker, Rev. Mod. Phys. **80**, 1337 (2008).

[18] N. Stander, B. Huard, and D. Goldhaber-Gordon, Phys. Rev. Lett. **102**, 026807 (2009).

[19] A. Rycerz, J. Tworzydlo, and C. W. J. Beenakker, Nat. Phys. **3**, 172 (2007); L. A. Ponomarenko, F. Schedin, M. I. Katsnelson, R. Yang, E. W. Hill, K. S. Novoselov, and A. K. Geim, Science **320**, 356 (2008); X. Du, I. Skachko, and E. Y. Andrei, Phys. Rev. B **77**, 184507 (2008); V. Pereira and A. Castro Neto, arXiv:0810.4539 (unpublished).

[20] X. Wang, Y. Ouyang, X. Li, H. Wang, J. Guo, and H. Dai, Phys. Rev. Lett. **100**, 206803 (2008).

[21] Y.-M. Lin, K. A. Jenkins, A. Valdes-Garcia, J. P. Small, D. B. Farmer, and P. Avouris, Nano Lett. **9**, 422 (2009).

[22] For a review, see P. Avouris, Z. Chen, and V. Perebeinos, Nat. Nanotechnol. **2**, 605 (2007).

[23] C. Berger *et al.*, Science **312**, 1191 (2006); M. D. Fischbein and M. Drndić, Appl. Phys. Lett. **93**, 113107 (2008).

[24] F. Molitor, J. Güttinger, C. Stampfer, D. Graf, T. Ihn, and K. Ensslin, Phys. Rev. B **76**, 245426 (2007).

[25] A. J. M. Giesbers, G. Rietveld, E. Houtzager, U. Zeitler, R. Yang, K. S. Novoselov, A. K. Geim, and J. C. Maan, Appl. Phys. Lett. **93**, 222109 (2008).

[26] D.-K. Ki, D. Jeong, J.-H. Choi, H.-J. Lee, and K.-S. Park, Phys. Rev. B **78**, 125409 (2008).

[27] A. K. Geim and K. S. Novoselov, Nature Mater. **6**, 183 (2007).

[28] M. Y. Han, B. Ozyilmaz, Y. Zhang, and P. Kim, Phys. Rev. Lett. **98**, 206805 (2007).

[29] Y.-M. Lin, V. Perebeinos, Z. Chen, and P. Avouris, Phys. Rev. B **78**, 161409(R) (2008).

[30] C. Stampfer, J. Güttinger, S. Hellmüller, F. Molitor, K. Ensslin, and T. Ihn, Phys. Rev. Lett. **102**, 056403 (2009).

[31] S. Russo, J. B. Oostinga, D. Wehenkel, H. B. Heersche, S. S. Sobhani, L. M. K. Vandersypen, and A. F. Morpurgo, Phys. Rev. B **77**, 085413 (2008).

[32] T. G. Pedersen, C. Flindt, J. Pedersen, N. A. Mortensen, A.-P. Jauho, and K. Pedersen, Phys. Rev. Lett. **100**, 136804 (2008).

[33] T. G. Pedersen, C. Flindt, J. Pedersen, A.-P. Jauho, N. A. Mortensen, and K. Pedersen, Phys. Rev. B **77**, 245431 (2008).

[34] T. Shen, Y. Q. Wu, M. A. Capano, L. P. Rokhinson, L. W. Engel, and P. D. Ye, Appl. Phys. Lett. **93**, 122102 (2008).

[35] J. Eroms and D. Weiss, arXiv:0901.0840 (unpublished).

[36] O. V. Yazyev, Phys. Rev. Lett. **101**, 037203 (2008).

[37] J. J. Palacios, J. Fernández-Rossier, and L. Brey, Phys. Rev. B **77**, 195428 (2008); J. Fernández-Rossier and J. J. Palacios, Phys. Rev. Lett. **99**, 177204 (2007).

[38] S. Hikami, A. I. Larkin, and Y. Nagaoka, Prog. Theor. Phys. **63**, 707 (1980); F. Pierre and N. O. Birge, Phys. Rev. Lett. **89**, 206804 (2002).

[39] E. H. Lieb, Phys. Rev. Lett. **62**, 1201 (1989).

[40] M. Inui, S. A. Trugman, and E. Abrahams, Phys. Rev. B **49**, 3190 (1994).

[41] N. Shima and H. Aoki, Phys. Rev. Lett. **71**, 4389 (1993).

[42] S. Reich, J. Maultzsch, C. Thomsen, and P. Ordejón, Phys. Rev. B **66**, 035412 (2002).

[43] K. Hannewald, V. M. Stojanović, J. M. T. Schellekens, P. A. Bobbert, G. Kresse, and J. Hafner, Phys. Rev. B **69**, 075211 (2004).

[44] G. Binnig and H. Rohrer, Rev. Mod. Phys. **71**, S324 (1999).

[45] See, for example, G. Grosso and G. P. Parravicini, *Solid State Physics* (Academic, New York, 2003), p. 20.

[46] P. Fazekas, *Lecture Notes on Electron Correlation and Magnetism* (World Scientific, New York, 1999).

[47] M. Fujita, K. Wakabayashi, K. Nakada, and K. Kusakabe, J. Phys. Soc. Jpn. **65**, 1920 (1996).

[48] K. Nakada, M. Fujita, G. Dresselhaus, and M. S. Dresselhaus, Phys. Rev. B **54**, 17954 (1996).

[49] K. Kusakabe and M. Maruyama, Phys. Rev. B **67**, 092406 (2003).

[50] Similar midgap states have recently been shown to lead to an order-of-magnitude increase in conductance in graphene; see S. Jafri, K. Carva, E. Widenkvist, T. Blom, B. Sanyal, J. Fransson, O. Eriksson, U. Jansson, H. Grennberg, O. Karis, R. Quinlan, B. Holloway, and K. Leifer, arXiv:0905.1346 (unpublished).

[51] R. E. Peierls, Z. Phys. **80**, 763 (1933).

[52] D. A. Bahamon, A. L. C. Pereira, and P. A. Schulz, Phys. Rev. B **79**, 125414 (2009).

[53] This is, indeed, intuitively plausible from the point of view of the standard first-order Rayleigh-Schrödinger perturbation theory of a degenerate energy level; see, for example, L. D. Landau and E. M. Lifshitz, *Quantum Mechanics*, Course of Theoretical Physics Vol. 3 (Pergamon, Oxford, 1991).

[54] S. Nishino, M. Goda, and K. Kusakabe, J. Phys. Soc. Jpn. **72**, 2015 (2003); S. Miyahara, K. Kubo, H. Ono, Y. Shimomura, and N. Furukawa, *ibid.* **74**, 1918 (2005).

[55] Z. Liu, K. Suenaga, P. J. F. Harris, and S. Iijima, Phys. Rev. Lett. **102**, 015501 (2009).

[56] H. A. Mizes and J. S. Foster, Science **244**, 559 (1989).

[57] P. Ruffieux, O. Gröning, P. Schwaller, L. Schlapbach, and P. Gröning, Phys. Rev. Lett. **84**, 4910 (2000).

[58] G. M. Rutter, J. N. Crain, N. P. Guisinger, T. Li, P. N. First, and J. A. Stroscio, Science **317**, 219 (2007).

[59] Y. Kobayashi, K.-I. Fukui, T. Enoki, and K. Kusakabe, Phys. Rev. B **73**, 125415 (2006).

[60] Y. Hasegawa and P. Avouris, Phys. Rev. Lett. **71**, 1071 (1993).

[61] P. Mallet, F. Varchon, C. Naud, L. Magaud, C. Berger, and J.-Y. Veuillen, Phys. Rev. B **76**, 041403(R) (2007).